Electromagnetic Properties of Disordered Three-Dimensional Mixtures

AUSTIN J. PICKLES, IAN M. KILGORE (Member, IEEE), AND MICHAEL B. STEER (Fellow, IEEE)
Department of Electrical and Computer Engineering, North Carolina State University, Raleigh, NC 27695, USA
Corresponding author: A. J. Pickles (ajpickle@ncsu.edu)

ABSTRACT The electromagnetic (EM) properties of two-component mixtures involving many disordered regularly and irregularly shaped crystals are studied. The effective relative permittivities are calculated utilizing the time-domain finite integration technique. The effective permittivity of disordered mixtures deviates from established mixing theories especially in cases of high permittivity contrast between inclusions and matrix material, and is strongly correlated to the cross-sectional area of the inclusion crystals. Electric energy density localizes at the edges and corners of inclusions in a manner independent of inclusion shape and influenced by EM propagation direction and surrounding inclusions. For mixtures with both disordered irregular and more organized cube inclusions, energy localization increases as the EM signal travels through the mixture before decreasing due to attenuation of the propagating EM signal. With a large number of inclusion crystals (here in the hundreds), it is found that the impact on effective permittivity from differences in individual inclusion shapes is negligible.

INDEX TERMS Composites, effective permittivity, electric energy density, electromagnetic propagation, energy localization, hotspot, mixing rules, mixtures, pulsed microwaves, random medium, relative permittivity, transient electromagnetic analysis.

I. INTRODUCTION

Natural and manufactured composites comprise two or more components, and while the electrical properties of the individual components may be well known, the electrical properties of a composite are generally thought to be dependent on the shape, orientation, surface structure, and distribution of components. An understanding of the electrical properties of component mixtures, including energy localization, is important in nondestructive testing, predicting the response of rocket fuel and explosives to electromagnetic (EM) insult, remote sensing, and in industrial heating and curing.

The EM behavior of such a non-magnetic complex object is largely described by its effective permittivity. Studies of effective medium properties have used various simulation methods. The effective permittivity of a mixture has been calculated using finite difference time-domain EM simulation in two dimensions [1], [2] and three dimensions [3], [4], in two dimensions using frequency-domain finite element EM analysis [5], and in three dimensions using the frequency-domain finite difference [6]–[8] and finite element [9]–[11] methods.

The random combination of variously shaped inclusions with a permittivity contrast to the embedding matrix can result in macroscopic anisotropy. The standard electrical characterization procedure is then to average the effective permittivity calculated in each of three orthogonal directions to obtain an overall effective permittivity of the mixture [9]–[12].

Earlier studies considered a single type of inclusion in a matrix material with permittivity contrasts between inclusion and matrix of up to 10 to 1 [2], [3]. These studies were limited to a few inclusions because of computational complexity, and found that the effective permittivity depended on the shape of the inclusion. In an earlier paper [12] we studied the effective permittivities of mixtures modeled with a single irregular crystal shape using the Finite Integration Technique (FIT) and found deviation from established mixing theories that was especially significant with high permittivity contrast between inclusion and matrix material. This present paper models mixtures with hundreds of irregularly and regularly shaped inclusions in a disordered arrangement. The effective

permittivity results are compared to the predictions of classical mixing rules and to each other. It is shown here that with many inclusions (in the hundreds), even when there is relatively high permittivity contast between inclusion and matrix material of up to 28 to 1, the impact of inclusion shape on effective permittivity is negligible. In addition, mixtures with many irregular and regular crystals are studied to provide insight into how the combination of individual crystals within a larger mixture impacts EM energy localization and the creation of hotspots. Again it is seen that inclusion shape has little effect on energy localization behavior.

This paper provides a basis for understanding how pulsed microwave signals can be used to characterize materials and for understanding how pulsed microwave signals can create hotspots in materials either intentionally or inadvertently. For this reason EM analysis is performed in the time domain.

II. CLASSICAL MIXING RULES

The classical Maxwell Garnett mixing theory gives the effective permittivity, ϵ_{eff}, of a two-component three-dimensional mixture with spherical inclusions as [13]

$$\epsilon_{\text{eff}} = \epsilon_2 + 3q\epsilon_2 \frac{\epsilon_1 - \epsilon_2}{\epsilon_1 + 2\epsilon_2 - q(\epsilon_1 - \epsilon_2)}. \quad (1)$$

In (1) ϵ_1 is the inclusion permittivity, ϵ_2 is the matrix material permittivity, and q is the filling factor (i.e., the volume fraction of the inclusions). The quasistatic assumption inherent to the development of (1) is that the inclusion size is much smaller than the EM wavelength so that the effective permittivity is independent of frequency. The Maxwell Garnett mixing theory also assumes spherical non-touching inclusions that are far apart [9], [12].

The classical Bruggeman mixing theory in three dimensions and for spherical inclusions is [14]

$$(1-q)\frac{\epsilon_2 - \epsilon_{\text{eff}}}{\epsilon_2 + 2\epsilon_{\text{eff}}} + q\frac{\epsilon_1 - \epsilon_{\text{eff}}}{\epsilon_1 + 2\epsilon_{\text{eff}}} = 0. \quad (2)$$

In effect, the Bruggeman rule for the effective permittivity weights the contribution of the inclusions by q and that of the matrix material by $(1 - q)$ [12], [15].

The Maxwell Garnett and Bruggeman mixing laws can be combined into one uniform equation [6], [11]:

$$\frac{\epsilon_{\text{eff}} - \epsilon_2}{\epsilon_{\text{eff}} + 2\epsilon_2 + \nu(\epsilon_{\text{eff}} - \epsilon_2)} = q\frac{\epsilon_1 - \epsilon_2}{\epsilon_1 + 2\epsilon_2 + \nu(\epsilon_{\text{eff}} - \epsilon_2)}. \quad (3)$$

where ν is a parameter used to describe a given mixing equation. Maxwell Garnett can be obtained with $\nu = 0$ and Bruggeman with $\nu = 2$ [6], [11]. However, the classical mixing rules are not directly applicable to mixtures with arbitrarily shaped inclusions [9], [12].

The maximum, $\epsilon_{\text{eff,max}}$, and minimum, $\epsilon_{\text{eff,min}}$, possible effective permittivities of a mixture are described by the Wiener bounds [1], [6], [11]:

$$\epsilon_{\text{eff,max}} = q\epsilon_1 + (1-q)\epsilon_2 \quad (4)$$

$$\epsilon_{\text{eff,min}} = \frac{\epsilon_1 \epsilon_2}{q\epsilon_2 + (1-q)\epsilon_1}. \quad (5)$$

These maximum and minimum Wiener bounds for permittivity correspond to capacitors in a circuit connected in parallel or series respectively [1], [6]. These bounds are also applicable when the permittivities of the components are complex [16].

III. METHOD OF SIMULATION

Calculated or measured scattering (S-) parameters can be employed to find the effective permittivity of a sample with a finite thickness d [12], [17]–[20]. Here these S-parameters are derived from a time-domain EM analysis using a Gaussian excitation pulse. In particular, CST Microwave Studio [21], utilizing the time-domain finite integration technique (FIT) with hexahedral meshing, is used for EM simulations. To confirm the accuracy of the simulations, the number of mesh cells was increased until the effective permittivity converged to an asymptotic value. To achieve a change in effective permittivity of less than 1%, at least 5,000,000 mesh cells were required. Computation used an 80 core machine with 160 GB of RAM and clocking at 2.66 GHz.

The refractive index n of a sample of length d in the propagation direction can be calculated from the S-parameters (for excitation at Port 1) as [12], [19], [20]:

$$n = \pm \left\{ \frac{1}{kd}\arccos\left[\frac{1}{2S_{21}}(1 - S_{11}^2 + S_{21}^2)\right] + \frac{2\pi m}{kd} \right\}, \quad (6)$$

where the free space wavenumber $k = \omega/c$, ω is the angular frequency, and c is the speed of light. The integer m indicates that multiple solutions are possible. Also, the relative wave impedance z is defined as [12], [19], [20]:

$$z = \pm\sqrt{\frac{(1 + S_{11})^2 - S_{21}^2}{(1 - S_{11})^2 - S_{21}^2}}. \quad (7)$$

In (6) and (7) the S-parameters are normalized to the impedance of free space, η. When d and the wavelength λ are comparable, obtaining a unique result for n can be difficult. However in this paper d is less than $\lambda/4$ at the frequency analyzed, 1 GHz, so a unique result for n can be found and the default branch is used with $m = 0$ and positive n in (6). With a passive material $\Re(z)$ is positive, so in (7) the positive branch is taken. These solutions for n and z can be used to find the unambiguous effective permittivity for a nonmagnetic mixture as [12], [19], [20]:

$$\epsilon_{\text{eff}} = \frac{n}{z}. \quad (8)$$

From [19], the calculations in (6) and (7) utilize the transmission and reflection coefficients for the mode that is propagating, which, for the situation analyzed in this paper, is TEM through 50 GHz.

IV. MULTIPLE CRYSTAL MIXTURES

In this section the effective permittivity of various two-component mixtures is derived. The mixtures have variously shaped crystal inclusions having first low and then high permittivity contrast with the embedding matrix. The mixtures

involving many irregular and cube-shaped crystals created in the CST Microwave Studio environment were defined using an automatic procedure based on computer gaming software [22]. In particular, a computer game was created in which crystals (the inclusions) were poured into a box and the physics engine of the game [23] modeled the jostling and bouncing of the crystals as they packed under gravity.

A. CRYSTAL STRUCTURES IN CST MICROWAVE STUDIO

The irregular crystals used as inclusions have a maximum size of 0.19 mm as used in [12]. A scaling factor in the range of 0.1 to 1 (and so the crystal sizes are much smaller than a wavelength at 50 GHz) was then used to randomly assign sizes to each crystal. The different scaling factors for each crystal create a structure with an array of crystal sizes but each crystal has the same shape. An example of a complex mixture with irregularly shaped crystal inclusions in the CST Microwave Studio environment is given in Fig. 1. Additional mixtures were created still exhibiting a disordered arrangement of crystals, but this time with crystals shaped as cubes. An example of such a structure is shown in Fig. 2. In both Figs. 1 and 2 none of the crystals are touching (a separation that can be controlled) and the crystals are surrounded by matrix material with a relative permittivity of 1.
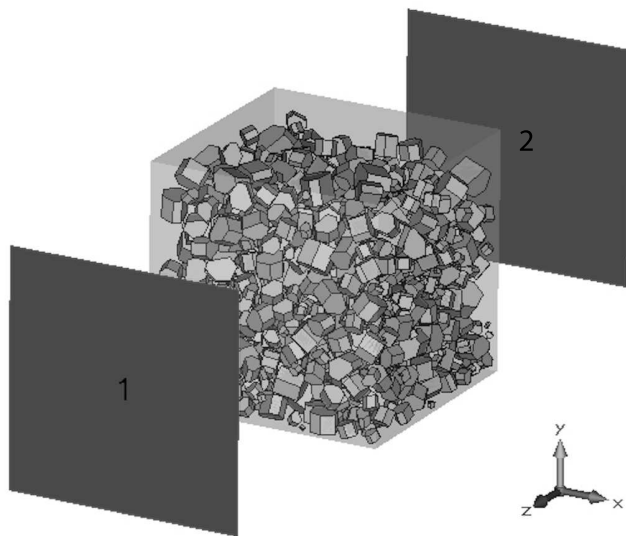
FIGURE 1. A total of 978 irregularly shaped inclusion crystals inside of a block (with side length of 1.37 mm) in a TEM simulation environment. The volume fraction of the inclusions is 27.5%.

EM propagation through the materials was modeled by placing the structures into a parallel plate transverse EM (TEM) environment [2], [12]. Waveguide excitation Ports 1 and 2 are defined on the propagation axis, the z axis in Figs. 1 and 2, and perfectly matched layer (PML) boundary conditions at the x-y boundaries. This eliminated reflections from the boundary planes back into the TEM structure. With the crystal structure fixed, but with the boundary conditions changed appropriately, propagation in the x and y directions
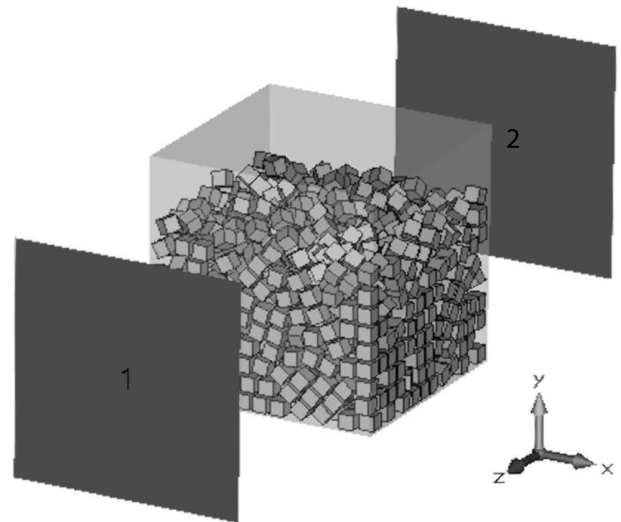
FIGURE 2. A total of 1,144 disordered cube inclusion crystals (each with side length of 0.085 mm) inside of a vacuum outer block (with side length of 1.37 mm). The volume fraction of inclusions is 27.5%.

were also analyzed. To obtain the S-parameters to be used in (6) and (7), measurements were de-embedded to the surface of the cubes in Figs. 1 and 2. Effective permittivity was then determined using (8) and a Gaussian pulse excitation signal with frequency content up to 50 GHz, as in [12].

B. LOW PERMITTIVITY INCLUSIONS

First, irregularly and cube shaped inclusions of mica-like crystals having low relative permittivity were considered to establish a lower permittivity contrast scenario between matrix and inclusions. Specifically, mica has a relative permittivity of 5.4 and a tan δ of 0.0006 measured at 1 GHz [24]. Propagation was analyzed for each orthogonal propagation axis, representing E_x, E_y, and E_z polarizations. These results were then averaged to obtain a single effective permittivity (as described in [7], [8], [11], and [12]). Results of effective permittivity at 1 GHz are compared to the Maxwell Garnett and Bruggeman mixing theories and the Wiener bounds in Fig. 3.

Fig. 3 indicates that the simulated effective permittivities for the low permittivity contrast situation are close to the results predicted by Bruggeman up to a 40% volume fraction. (This volume fraction is approximately the limit of what can be obtained using irregularly shaped crystals of various sizes [22].) The simulated effective permittivities for the cube crystals and the irregularly shaped crystals at the same volume fraction differ by less than 0.5%. This indicates that, with low permittivity contrast, the effective permittivity of mixtures with many inclusions in a disordered arrangement has very little dependence on inclusion shape.

C. HIGH PERMITTIVITY INCLUSIONS

The above simulations were repeated with the same structures, but this time with inclusion crystals of a higher permittivity yielding a higher permittivity contrast with the
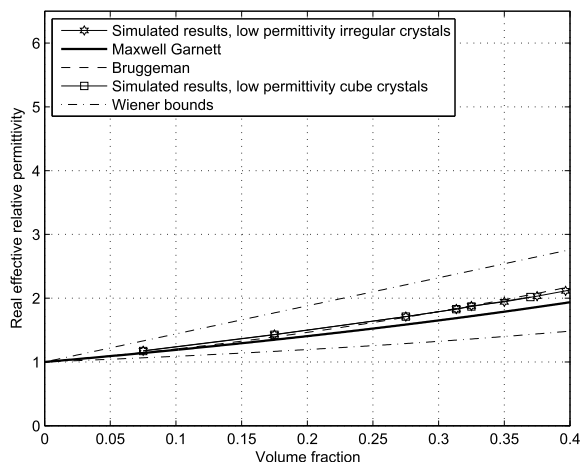
FIGURE 3. Plots of real effective relative permittivity, $\Re(\epsilon_{eff})$, versus various filling factors for low permittivity irregular and cube inclusion crystals along with various mixing theories.

matter material. To represent zirconia-like inclusions the crystals now have a relative permittivity of 28 with a tan δ of 0.0009 taken at 1 GHz [12], [24]. Results of effective permittivity at 1 GHz for irregularly shaped and cube inclusions are given in Fig. 4.
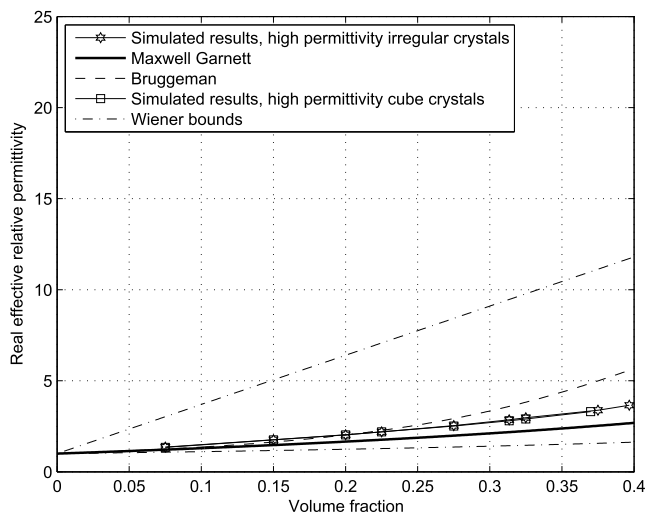

FIGURE 4. Plots of real effective relative permittivity, $\Re(\epsilon_{eff})$, as a function of filling factor for high permittivity irregular and cube inclusion crystals along with various mixing theories.

In Fig. 4 the simulated results fall within the Wiener bounds as expected. The effective permittivities for the irregular inclusions and cube inclusions for this high contrast situation also fall between the results predicted by Maxwell Garnett and Bruggeman and are very close to each other. Numerically, of the eight simulated volume fractions for the mixtures with cube inclusions (as can be seen in Fig. 4), six differ from the irregular inclusion results on average by 1% or less. The greatest percent difference is 2.5% (with an absolute difference in effective permittivity of approximately 0.07

occuring at 32.5% volume fraction). Fig. 4 shows that even with a high permittivity contrast (here 28 to 1), the effective permittivity of composite mixtures with hundreds of disordered crystals still has very little dependence on inclusion shape. Earlier research [2], [3], [7] has shown significant differences in effective permittivity between inclusions of different shapes for single-inclusion mixtures. Also, there was no significant convergence in the effective permittivity results when up to eight of each type of inclusion were analyzed [3].

V. OVERALL INCLUSION STRUCTURE AND PERMITTIVITY
This section explores in greater detail how the overall arrangement of inclusions influences the individual extracted effective permittivity components (i.e., $\epsilon_{eff,x}$, $\epsilon_{eff,y}$, and $\epsilon_{eff,z}$ components in the x, y, and z directions respectively) of a mixture.

A. HIGH PERMITTIVITY INCLUSIONS
The scenarios that lead to the maximum and minimum possible effective permittivity, as described by the Wiener bounds, are when the inclusion material has the shape of a plate [1]. For example, a structure having an effective permittivity corresponding to the upper Weiner bound is given in Fig. 5.
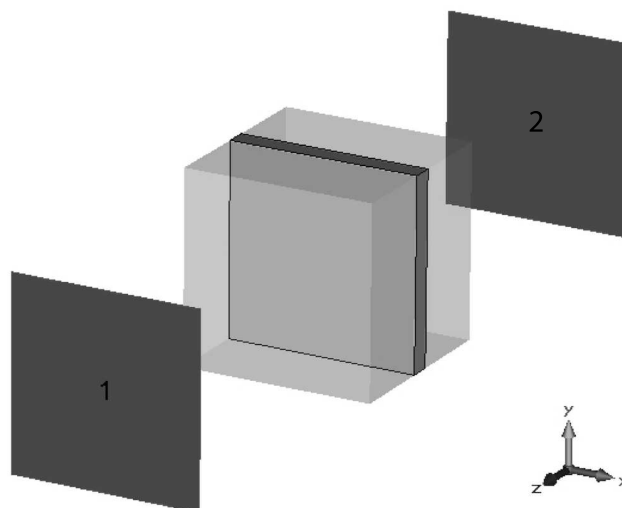

FIGURE 5. Structure showing a high permittivity inclusion arranged as a plate in vacuum with 11.0% volume fraction.

In Fig. 5, the side length of the outer box is 0.91 mm and the thickness of the plate in the z direction is 0.10 mm, giving a volume fraction of 11.0%. The Wiener bounds from (4) and (5) can be used to find the maximum and minimum effective permittivity possible. For the structure in Fig. 5, these bounds are found to be 3.97 for the maximum $\Re(\epsilon_{eff})$ and 1.12, changing the propagation direction, for the minimum $\Re(\epsilon_{eff})$.

These results will now be compared to the simulated effective permittivities. For the structure in Fig. 5 the extracted effective permittivity depends on the axis of the electric field polarization. The structure in Fig. 5 has the same electrical

properties for *x*- and *y*-directed electric fields. For *x* and *y* polarization $\Re(\epsilon_{\mathrm{eff}})$ from simulation was found to be identical, i.e. 3.97. Notably, this corresponds to the maximum Wiener bound. For *z*-directed electric field, $\Re(\epsilon_{\mathrm{eff}})$ from simulation was found to be 1.13, nearly identical to the minimum Wiener bound.

So, as described in [1], these results confirm that the maximum effective permittivity at a given volume fraction occurs when the largest face of the inclusion plate is parallel to the electrical polarization of the TEM field. The minimum effective permittivity occurs when the largest face of the inclusion plate is perpendicular to the electrical polarization of the TEM field.

B. RELATIONSHIP TO CROSS-SECTIONAL AREA
In an effort to relate the arrangement of the plate in Fig. 5 to the maximum or minimum effective permittivity, the cross-sectional areas of the inclusion from Fig. 5 are studied. Analyzing Fig. 5, the maximum effective permittivity occurs when the inclusion has the minimum possible cross-sectional area normal to the direction of the electric field polarization. In this scenario, the narrow edge of the plate is 'seen' first by the electric field. Conversely, the minimum effective permittivity occurs when the inclusion has the maximum possible cross-sectional area normal to the electric field polarization direction. Here, the wide face of the plate is presented to the incident electric field. So, this suggests that, for an inclusion shaped as a plate, there is an inverse relationship between the presented cross-sectional area of the inclusion and the effective permittivity of the mixture. This conclusion is consistent with our previous research [12] where a similar inverse relationship between effective permittivity and cross-sectional area was developed for a single arbitrarily shaped inclusion crystal.

To investigate the cross-sectional area relationship for structures containing many inclusions, a mixture containing irregular crystals with a 15% volume fraction, as shown in Fig. 6, and a mixture containing cube crystals also with a 15% volume fraction, as shown in Fig. 7, were considered. Cross-sectional area was calculated using rays cast along the appropriate axis using the Bullet physics library [23]. For example, to determine the cross-sectional area presented by crystals from the perspective of the *x* axis, the *y-z* face of the outer box is divided into an $N \times N$ grid (here $N = 500$). For every point on the grid, a ray is cast perpendicularly to the *y-z* face (in the *x* direction) from one side of the outer box to the other. If the ray hits a crystal, a hit is recorded. The cross-sectional area of the crystals, A_{crystals}, is then defined as:

$$A_{\mathrm{crystals}} = nA_{\mathrm{cell}}, \tag{9}$$

where *n* is the number of hits and A_{cell} is the area of one grid cell. The cross-sectional area fraction, A_w, (*w*=*x*, *y* or *z*) is further defined for a given axis perspective (the *x* direction is used as an example here) as:

$$A_x = \frac{A_{\mathrm{crystals}}}{A_{\mathrm{total}}}, \tag{10}$$

where A_{total} is the total area of the outer box. The cross-sectional area of crystals and cross-sectional area fraction are calculated in this manner for the *x*, *y*, and *z* directions independently.
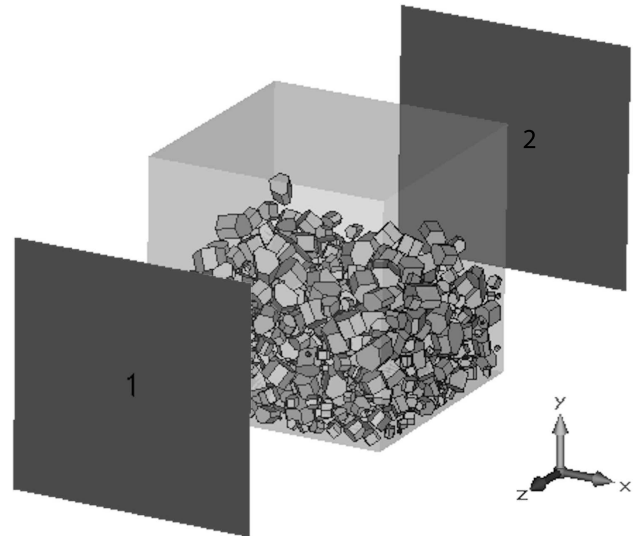

FIGURE 6. Structure showing 894 high permittivity irregular inclusions inside a vacuum outer block (with side length 1.46 mm). The volume fraction of inclusions is 15%.
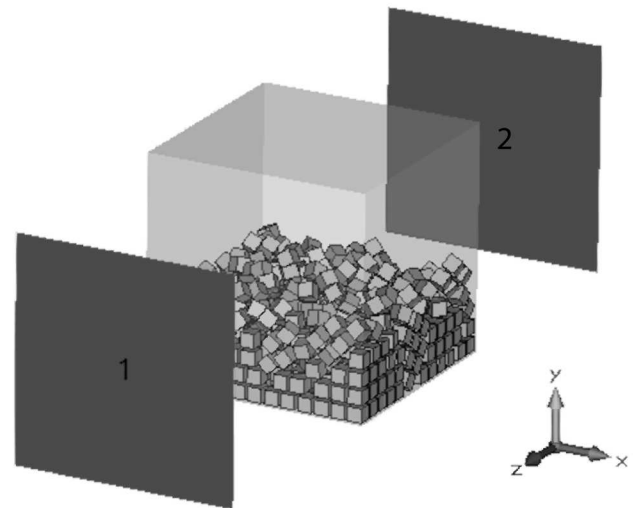
FIGURE 7. Structure showing 624 high permittivity cube inclusions (each with side length 0.085 mm) inside a vacuum outer block (with side length 1.37 mm). The volume fraction of inclusions is 15%.

With high permittivity inclusions at 15% volume fraction, the effective permittivities and corresponding cross-sectional area fractions, A_w, for each axis are given in Fig. 8. Comparing all cases presented in Fig. 8, the highest cross-sectional area fraction value corresponds to the lowest effective permittivity component and vice versa, suggesting an inverse relationship.

The differences in magnitude of the effective permittivity among the polarizations as presented in Fig. 8 can be
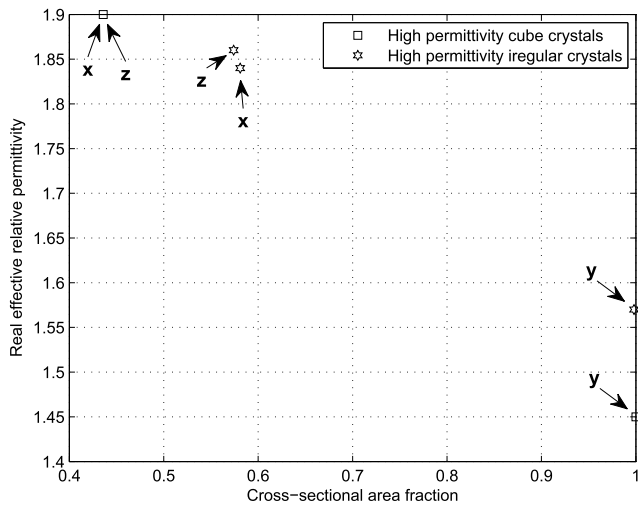
FIGURE 8. Real effective permittivity, $\Re(\epsilon_{\mathrm{eff}})$, plotted as a function of cross-sectional area fraction, A_W. The volume fraction of inclusions is 15%. The letters near the data points indicate the electric field polarization axis for each type of crystal as well as the cross-sectional area fraction direction.

qualitatively related to the cross-sectional area fraction differences by analyzing the mixtures in Figs. 6 and 7. Based on the way the irregular structures are created using the Bullet physics library, the crystals fall from above (with respect to the y axis) and fall to the bottom of the outer box before settling. The crystals therefore become tightly packed on the bottom of the box as can be seen in Figs. 6 and 7.

This means that from the perspective of the y axis, the inclusion crystals have a high cross-sectional area fraction, A_y. From the perspective of the x and z axes, the cross-sectional areas of the inclusions are relatively small and so A_x and A_z are smaller. This can also be seen in Figs. 6 and 7, where from the perspective of the x and z axes the upper part of the box is the background material (with relative permittivity of 1).

Relating this to the permittivity values, a high A_W from the perspective of the TEM electric field polarization axis, w, leads to a low effective permittivity (e.g. here A_y is high and the effective relative permittivity component in the y direction, $\epsilon_{\mathrm{eff},y}$, is low) while the other polarizations have lower A_W and higher effective permittivity. This is the same inverse relationship demonstrated by the plate of Fig. 5. Since the crystals do not form a complete plate in any direction, the maximum or minimum possible permittivity values as given by the Wiener bounds are not reached. However, based on the way the crystals are packed in the box in Figs. 6 and 7, they are quite dense and close to the sides of the box. In this situation it can be said that the inclusions exhibit plate-like behavior. This can be seen through the sharing of an inverse relationship between cross-sectional area fraction and effective permittivity for both the plate and the densely packed crystals. This correspondence is seen for all of the simulation results for low and high permittivity inclusions presented in Figs. 3 and 4 respectively. Since all of the simulations

covering the various volume fractions in Figs. 3 and 4 were created in the same manner (the crystals falling into the box along the y axis and then settling) A_w for all simulations was greatest looking along the y axis (i.e. $w=y$), and E_y polarization always yielded the smallest effective permittivity component.

VI. ENERGY LOCALIZATION

The other important phenomenon that characterizes the electrical response to a pulsed microwave signal is energy localization, in particular the concentration of electric energy in a nonmagnetic composite. Composites respond to temporal energy localization by delaminating and changing chemical phase. Also, identifying energy localization can be used as a diagnostic tool. Many of these effects respond over a short time interval so that it is the transient time-domain electromagnetic response that is more important than the steady-state response provided by a frequency-domain EM analysis. Energy has been found to localize on the edges and corners of single inclusions [2], [12]. This section explores localization phenomena taken using time-domain monitors for mixtures containing many crystals close together, highlighting phenomena neglected by steady-state analyses.
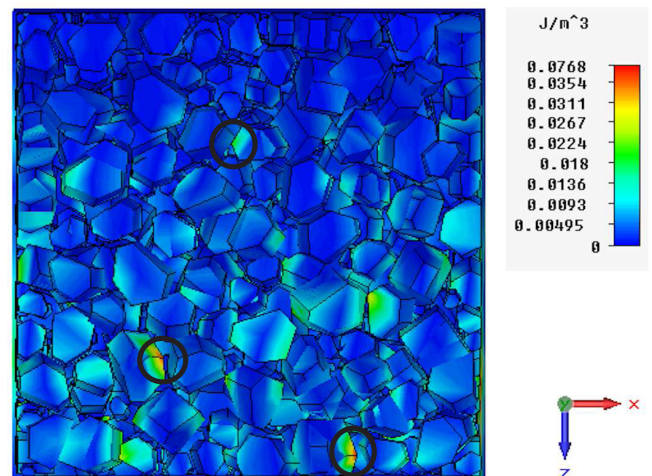

FIGURE 9. Near-maximum electric energy density showing localization at inclusion corners and edges, with highest localization in the bottom two circles. The electric field is polarized along the x axis and the propagation direction is positive z (down). The volume fraction is 32.5%.

A. HIGH PERMITTIVITY INCLUSIONS

First, electric energy density is plotted for a complex mixture with 32.5% volume fraction. An example showing near-maximum electric energy density in a high permittivity (with a real relative permittivity of 28) inclusion mixture for electric field polarized along the x axis and positive z propagation direction is given in Fig. 9. The excitation signal is a Gaussian pulse with frequency content up to 50 GHz. The near-maximum energy density is shown in Fig. 9 at 48.1 ps. The energy localizes to the greatest extent on the edges and corners of the irregular inclusions shown inside the bottom

two circles in Fig. 9 after the signal has passed through many other inclusions. Propagation in the reverse direction, along the negative z axis (up), results in the near-maximum electric energy density scenario in Fig. 10. This image is taken at the same time and plane as the structure shown in Fig. 9. The only difference in simulation conditions between Figs. 9 and 10 is an opposite direction of propagation.
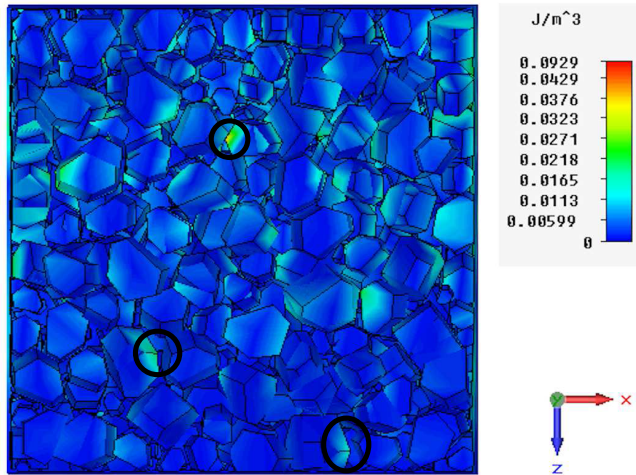
FIGURE 10. Electric energy density with the same conditions as in Fig. 9, but with propagation in the reverse direction (up). The strong localization from Fig. 9 is not seen in the bottom two circles. Instead, there is higher localization in the top circle.
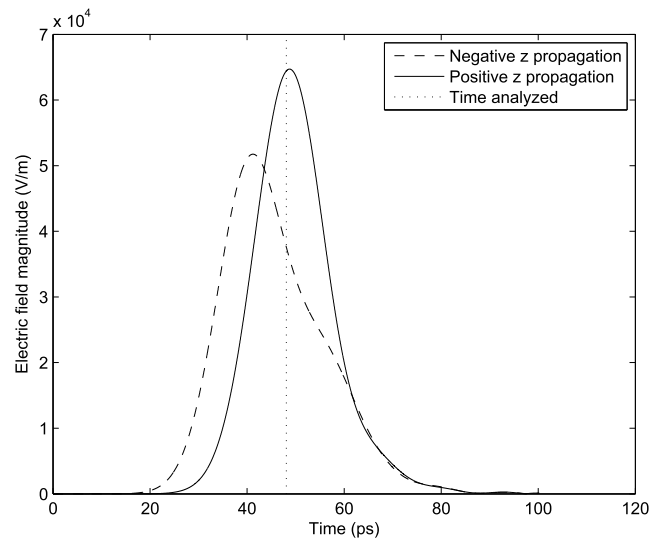
The crystal indicated by the upper circle in Fig. 10 shows greater energy density compared to the same location in Fig. 9. Conversely, the energy density on the crystals indicated by the bottom two circles is smaller. Comparing Figs. 9 and 10, the electric energy density localizes with different magnitudes depending on the direction of propagation of the EM signal. At specific locations, indicated by the black circles in Figs. 9 and 10, the magnitude of the energy density at the edges and corners is higher when the signal has traveled through more scatterers. As an additional test, the Gaussian pulse duration was extended so that the frequency content ranged from 0 to 25 GHz, and the energy was seen to localize in the same locations with the same localization behavior as for the 0 to 50 GHz bandwidth excitation used in Figs. 9 and 10.

The physical interpretation is that the energy localization maximum occurs when signals following multiple scattering paths coalesce at the same time and position. Such a hotspot is unlikely to occur at the surface of a composite but within the material after multiple scattering events have occurred but before the signal has been significantly attenuated.

B. ELECTRIC FIELDS FOR IRREGULAR INCLUSIONS
To gain a better understanding of the localization behavior occurring in the circles in Figs. 9 and 10, simulation probes were inserted to measure the electric field magnitudes over the course of the simulation. The electric fields at the location indicated by the bottom right circles in Figs. 9 and 10 are

given in Fig. 11, at the bottom left circles are given in Fig. 12, and at the top circles are given in Fig. 13. In Figs. 11–13, the electric field localizes at specific crystal corners and edges to a greater amount when the EM signal has previously traveled through more scatterers. From Figs. 11 and 12, peak energy localization at the bottom crystals occurs after the signal has traveled from top to bottom. The energy density for this positive z propagation direction is shown in Fig. 9 at the time indicated in Figs. 11 and 12, i.e. 48.1 ps. From Fig. 13, peak localization at the top crystal occurs after the signal travels from bottom to top, with energy density for this negative z propagation direction at the time indicated in Fig. 13, 48.1 ps, given in Fig. 10. The electric field probes from Figs. 11–13 confirm the results of energy density from Figs. 9 and 10 that traveling through a greater number of inclusions increases localization magnitude at a specific location. Next, this behavior is studied for a simpler case of identical inclusions placed on an organized grid.
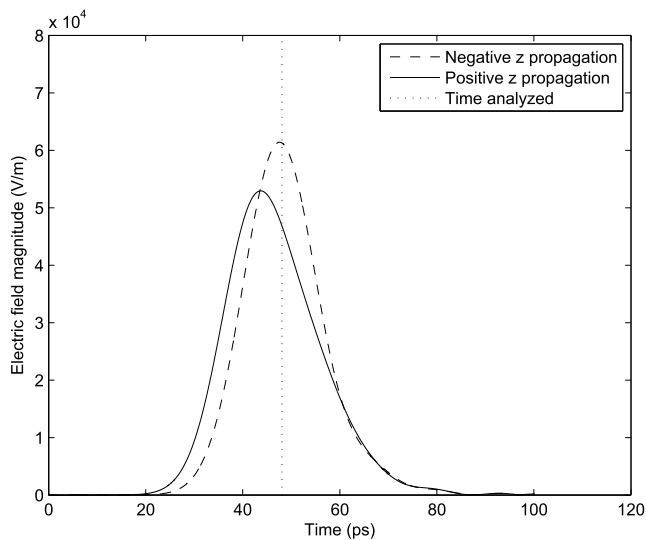

FIGURE 11. Comparison of the electric field at the crystal corner indicated by the bottom right circle in Figs. 9 and 10 with propagation direction. At 48.1 ps there is a significant difference in the electric field and electric energy density depending on propagation direction. Higher peak localization is seen with the positive propagation direction (down) when the EM signal has traveled through more of the irregular surrounding material.

C. BEHAVIOR FOR CUBE-SHAPED INCLUSIONS
From the previous section, the electric field localization magnitude was seen to increase when the EM signal traveled through a greater number of scatterers. This section studies electric field localization for a much less complicated mixture with high permittivity cube-shaped inclusions on a regular three-dimensional grid. The aim of this paper is to determine if a simpler simulation environment yields similar energy localization results. First, two parallel layers of cubes in the x-y plane are created as shown in Fig. 14. Each cube has a side length of 0.1 mm. The left x-y plane in Fig. 14 has 20 cubes placed randomly within the plane, two of which are referred to as the back cubes. After the cubes have been placed in the
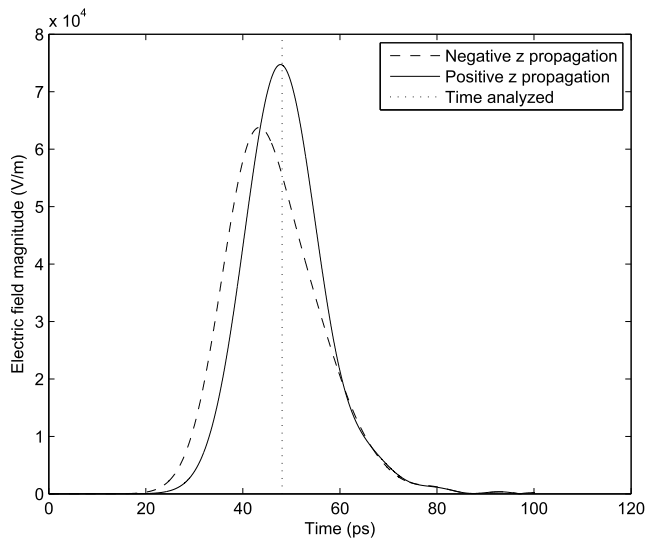
FIGURE 12. Comparison of the electric field at the crystal corner indicated by the bottom left circle in Figs. 9 and 10 with propagation direction. Higher peak localization is seen at 48.1 ps with the positive propagation direction (down) when the EM signal has traveled through more of the irregular surrounding material.


FIGURE 13. Comparison of electric field for the top circle in Figs. 9 and 10 with propagation direction. At 48.1 ps there is a significant difference in the electric field and electric energy density depending on propagation direction. Higher peak localization is seen with the negative propagation direction (up) when the EM signal has traveled through more of the irregular surrounding material.

plane, the back cubes (the two closest cubes in this plane) are then shifted in the positive *z* direction with the same *x* and *y* coordinates in order to maintain the same distance and orientation between the cubes but to isolate them in their own *x*-*y* plane. This pair of cubes, to be referred to as the isolated cubes, are shown on the right side of Fig. 14. The two cubes are isolated in order to study the influence of surrounding cubes within a plane on energy localization.

Next, additional cubes are placed in planes evenly spaced between those shown in Fig. 14. The resulting structure is
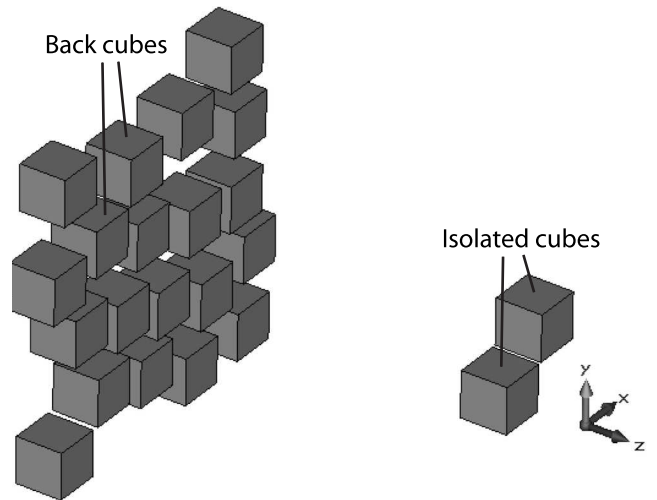
FIGURE 14. Cube-shaped inclusions arranged in two planes. On the right are the isolated cubes and on the left are the back cubes.
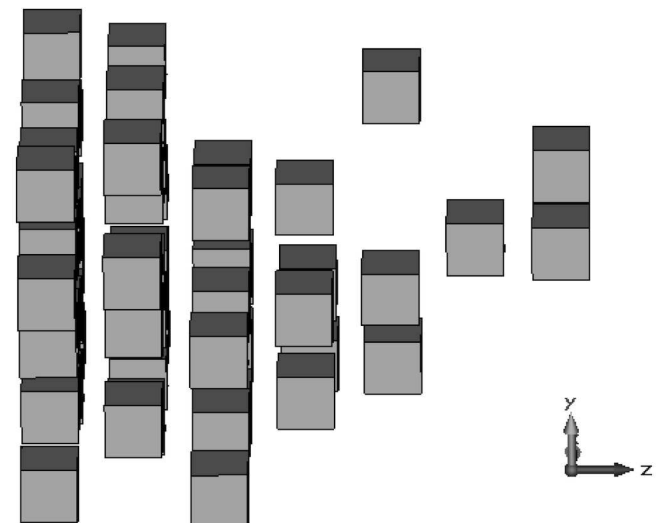

FIGURE 15. Layers of cube-shaped inclusions are added between the layers in Fig. 14 with an increasing number of inclusions in each layer.

shown in Fig. 15. The distance between cubes in two adjacent *x*-*y* planes in Fig. 15 is 0.05 mm and none of the cubes are touching. Behind the two isolated cubes on the right, going in the negative *z* direction (left), the next *x*-*y* plane has 1 cube, then 3, 5, 10, and 15 before the left-most plane with 20 cubes is reached. This gradually increases the number of inclusions between the layers shown in Fig. 14. The goal is to confirm the hypothesis that EM propagation through more inclusions leads to an increase in the peak hotspot magnitude.

The total structure with all cubes along with the waveguide Ports 1 and 2 is given in Fig. 16. In Fig. 16, the isolated cubes from Figs. 14 and 15 are closest to Port 1 and the back cubes are closest to Port 2. The two ports are the same distance to the nearest high permittivity cube in either direction, specifically 1.55 mm. The electric field is polarized along the *x* axis and *z* is the propagation axis. The excitation signal is a 0 to 50 GHz
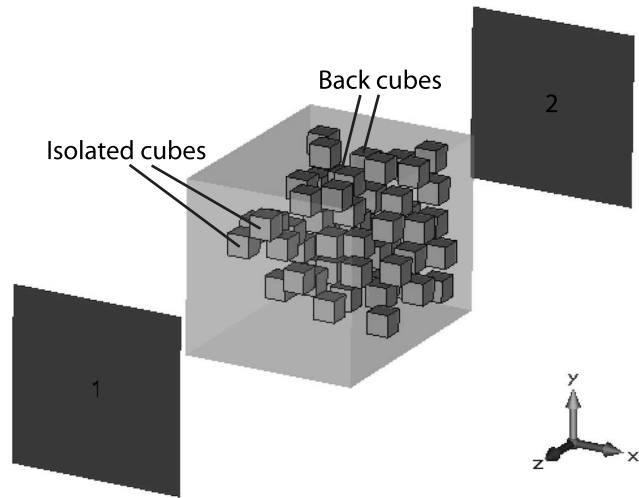
Gaussian pulse. The near-peak energy density location in the structure from Fig. 16 is shown in Fig. 17.
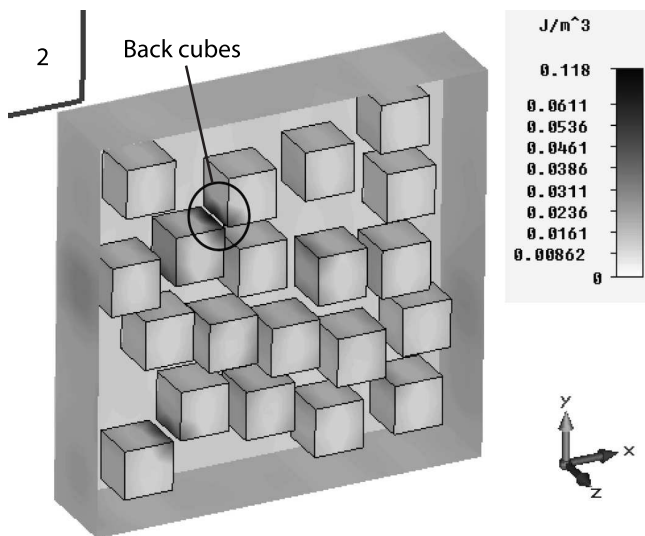
FIGURE 17. Near-peak electric energy density for the back layer of cubes at 44 ps (time of near-maximum energy density) with highest magnitude at the edges and corners of the back cubes as indicated by the black circle. This occurs for Port 1 excitation.

In Fig. 17, the highest energy density among all the cubes occurs at the edges and corners of the back cubes with Port 1 excitation. Again, localization magnitude is greater after the signal has traveled from Port 1 to Port 2 through a greater number of scatterers. The plane of cubes shown in Fig. 17 is the back layer with the highest number of cubes (20) closest to Port 2. The back cubes indicated by the black circle in Fig. 17 have edges and corners closest to each other within that plane, and no edges between other adjacent cubes are closer in the entire structure. So, adjacent cubes coming closer together also increases temporal energy localization.
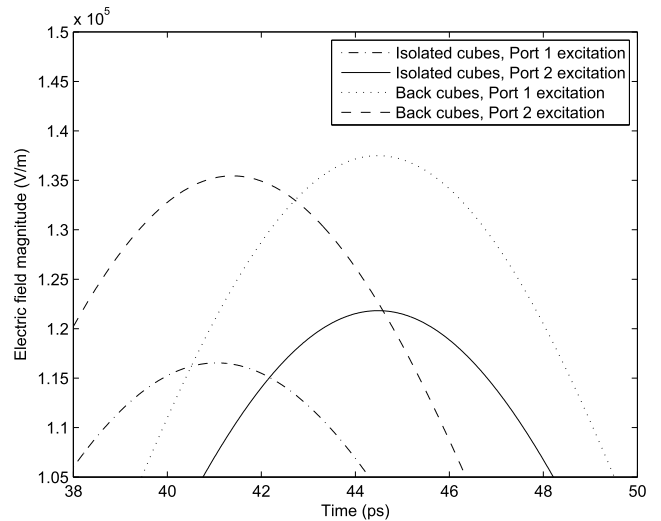
FIGURE 18. Electric field magnitudes for four different locations in the structure in Fig. 16 as a function of time. Peak localization magnitude is reached for the back cubes with Port 1 excitation after the signal has traveled through other scatterers.

Electric field probes can be used to gain an understanding of how the field magnitude changes over time. Probes are utilized to measure the electric field at the edge of one of the back cubes (encompassed by the circle in Fig. 17) as well as the same relative location but on the isolated pair of cubes closest to Port 1 (those indicated in Fig. 16). The results from these two probes, each probe measuring electric field with Port 1 and Port 2 excitation independently, are summarized in Fig. 18. The isolated cubes and back cubes referenced in Fig. 18 are analyzed because they represent the maximum EM localization within the mixture shown in Fig. 16. In Fig. 18, electric field localization magnitudes are plotted as a function of time. As shown in Fig. 14, there are two pairs of cubes with the same orientation to each other: the isolated cubes and the back cubes. One pair is surrounded by many other inclusions in the same plane (the back cubes shown in Fig. 14, in the plane of cubes closest to Port 2 in Fig. 16, and referenced in Fig. 18) and the other pair is isolated in a plane by itself (the isolated cubes shown in Fig. 14, in the plane of cubes closest to Port 1 in Fig. 16, and referenced in Fig. 18) to study the impact of surrounding inclusions. The two cubes within a pair are the same distance from each other and differ only in their z coordinates.

Analyzing Fig. 18, for the back cubes closely surrounded by other high permittivity cubes, the peak electric field magnitude is higher for both propagation directions (i.e. for Port 1 and Port 2 excitation, representing propagation in the negative and positive z directions respectively) than for either propagation direction for the isolated cubes in the front. There are more scatterers in the back layer, so the localization magnitude is higher than in the front where in that layer there are few scatterers. In summary, a greater number of scatterers within a layer increases energy localization.

For the back cubes in Fig. 18 (in the layer closest to Port 2 in Figs. 16 and 17), looking at the differences caused by changing the propagation direction, there is higher localization for Port 1 excitation than for Port 2 excitation. With excitation at Port 1, the signal goes through six layers of scatterers to get to the back layer (each layer can be seen independently in Fig. 15). Port 2 excitation means that the back layer is the first layer experienced by the signal. Since the EM field has not undergone previous scattering events, the magnitude of localization is lower for this propagation direction. Using the same reasoning as for the back layer, for the isolated cubes in Fig. 18 (closest to Port 1 in Fig. 16), Port 2 excitation yields higher localization because the signal travels through more scatterers before reaching the isolated cubes.

Also from Fig. 18 it is seen that the lowest overall localization magnitude occurs when the isolated cubes (i.e. few cubes in a layer) are the first scatterers encountered by the EM pulse. These are the isolated cubes closest to Port 1 in Fig. 16 with Port 1 excitation. Conversely, the highest overall localization magnitude occurs for the back cubes closest to Port 2 in Fig. 16 with Port 1 excitation (at the location encompassed by the circle in Fig. 17). In this situation there are the most scatterers within the layer and the signal has traveled through the highest number of scatterers to reach this back point close to Port 2.

In our previous research [12] we found energy localization on the edges and corners of a single irregular inclusion crystal. This paper studied energy density behavior for mixtures with many disordered irregular, as well as organized cube, inclusions. As the EM signal travels through more scatterers, the peak energy density has been shown to increase even if the inclusions are small compared to wavelength. These results suggest that a direct relationship exists between the disorder introduced by an increasing number of inclusions and localization magnitude.

VII. CONCLUSION

The effective EM properties for mixtures involving many disordered crystals were studied. In particular the crystal shape was found to have no appreciable impact on effective permittivity or energy localization behavior. The effective permittivity derived from simulations deviates from that calculated using conventional Maxwell Garnett and Bruggeman mixing theories. This departure is especially significant when there is a high permittivity contrast between the inclusions and the embedding matrix. This is so when the inclusions have irregular or regular shapes. For mixtures with hundreds of crystals the effect of individual inclusion shape and orientation on effective permittivity apparently averages out. As expected, inclusions in the form of a plate yield either maximum or minimum effective permittivity depending on the cross-section presented to the EM signal. In general a strong inverse relationship was found between the cross-sectional area presented by the inclusions and the effective permittivity of the mixture. While established mixing laws are functions of individual permittivity values and

volume fraction, this paper showed that cross-sectional area is also an important parameter to consider when determining the effective permittivity of mixtures of finite thickness.

Energy was seen to localize within mixtures containing many inclusions. The specific location of EM localization is on edges and corners of adjacent inclusions that are close to each other in the direction of electric field polarization. Temporal maximum energy density occurs only after appreciable scattering has occurred but before the EM signal has been attenuated.

REFERENCES

[1] K. K. Kärkkäinen, A. H. Sihvola, and K. I. Nikoskinen, "Effective permittivity of mixtures: Numerical validation by the FDTD method," *IEEE Trans. Geosci. Remote Sens.*, vol. 38, no. 3, pp. 1303–1308, May 2000.

[2] A. Mejdoubi and C. Brosseau, "Finite-difference time-domain simulation of heterostructures with inclusion of arbitrarily complex geometry," *J. Appl. Phys.*, vol. 99, pp. 063502-1–063502-14, Mar. 2006.

[3] D. Wu, J. Chen, and C. Liu, "Numerical evaluation of effective dielectric properties of three-dimensional composite materials with arbitrary inclusions using a finite-difference time-domain method," *J. Appl. Phys.*, vol. 102, pp. 024107-1–024107-8, Jul. 2007.

[4] D. Wu, R. Qiang, J. Chen, C. Liu, M. Koledintseva, J. Drewniak, *et al.*, "Numerical modeling of periodic composite media for electromagnetic shielding application," in *Proc. IEEE Int. Symp. EMC*, Jul. 2007, pp. 1–5.

[5] A. Mejdoubi and C. Brosseau, "Dielectric response of perforated two-dimensional lossy heterostructures: A finite-element approach," *J. Appl. Phys.*, vol. 100, pp. 094103-1–094103-14, Nov. 2006.

[6] K. K. Kärkkäinen, A. H. Sihvola, and K. I. Nikoskinen, "Analysis of a three-dimensional dielectric mixture with finite difference method," *IEEE Trans. Geosci. Remote Sens.*, vol. 39, no. 5, pp. 1013–1018, May 2001.

[7] M. Luo, C. Liu, and H. P. Pan, "Numerical simulation on dielectric enhancement of periodic composite media using a 3D finite difference method," *Eur. Phys. J. Appl. Phys.*, vol. 52, pp. 20501-1–20501-8, Sep. 2010.

[8] H. Wu, D. Wu, J. Chen, and R. Liu, "Evaluation of electrical properties for complex mixtures with a low-frequency periodic technique," in *IEEE MTT-S Int. Microw. Symp. Dig.*, Jun. 2008, pp. 1349–1352.

[9] Y. Cheng, X. Chen, K. Wu, S. Wu, Y. Chen, and Y. Meng, "Modeling and simulation for effective permittivity of two-phase disordered composites," *J. Appl. Phys.*, vol. 103, pp. 034111-1–034111-8, Feb. 2008.

[10] X. Chen, Y. Cheng, K. Wu, and S. Wu, "Interfacial polarization and its influence on effective complex permittivity of mixtures," in *Proc. ISEIM*, Sep. 2008, pp. 238–241.

[11] L. Jylhä and A. H. Sihvola, "Numerical modeling of disordered mixture using pseudorandom simulations," *IEEE Trans. Geosci. Remote Sens.*, vol. 43, no. 1, pp. 59–64, Jan. 2005.

[12] A. J. Pickles and M. B. Steer, "Effective permittivity of 3-D periodic composites with regular and irregular inclusions," *IEEE Access*, vol. 1, pp. 523–536, Aug. 2013.

[13] J. C. Maxwell Garnett, "Colours in metal glasses and in metallic films," *Phil. Trans. R. Soc. London Ser. A, Contain. Papers Math. Phys. Character*, vol. 203, nos. 359–371, pp. 385–420, Jan. 1904.

[14] D. A. G. Bruggeman, "The calculation of various physical constants of heterogeneous substances. I. The dielectric constants and conductivities of mixtures composed of isotropic substances," *Ann. Phys.*, vol. 24, no. 132, pp. 636–679, 1935.

[15] A. H. Sihvola, *Electromagnetic Mixing Formulas and Applications*. London, U.K.: IET, 1999, ch. 9, pp. 161–163.

[16] W. Cai and V. Shalaev, *Optical Metamaterials: Fundamentals and Applications*, New York, NY, USA: Springer-Verlag, 2010, ch. 4, pp. 60–64.

[17] A. M. Nicolson and G. F. Ross, "Measurement of the intrinsic properties of materials by time-domain techniques," *IEEE Trans. Instrum. Meas.*, vol. 19, no. 4, pp. 377–382, Nov. 1970.

[18] W. B. Weir, "Automatic measurement of complex dielectric constant and permeability at microwave frequencies," *Proc. IEEE*, vol. 62, no. 1, pp. 33–36, Jan. 1974.

[19] D. R. Smith, S. Schultz, P. Markoŝ, and C. M. Soukoulis, "Determination of effective permittivity and permeability of metamaterials from reflection and transmission coefficients," *Phys. Rev. B*, vol. 65, no. 19, pp. 195104-1–195104-5, Apr. 2002.

[20] N. C. Dyck, R. C. Denomme, and P. M. Nieva, "Effective medium properties of arbitrary nanoparticle shapes in a localized surface plasmon resonance sensing layer," *J. Phys. Chem. C*, vol. 115, no. 31, pp. 15225–15233, Jun. 2011.

[21] (2013). *CST Microwave Studio* [Online]. Available: http://www.cst.com/Content/Products/MWS/Overview.aspx

[22] A. J. Pickles, I. M. Kilgore, and M. B. Steer, "Automated creation of complex three-dimensional composite mixtures for use in electromagnetic simulation," *IEEE Access*, vol. 1, pp. 248–251, May 2013.

[23] E. Coumans. (2013). *Bullet Physics Library* [Online]. Available: http://bulletphysics.org/wordpress/

[24] M. B. Steer, *Microwave and RF Design: A Systems Approach*, 2nd ed. Raleigh, NC, USA: SciTech, 2013, pp. 1053–1056.

MICHAEL B. STEER (S'76–M'78–SM'90–F'99) received the B.E. (Hons.) and Ph.D. degrees from the University of Queensland, Queensland, Australia, in 1976 and 1983, respectively. He is currently the Lampe Distinguished Professor of electrical and computer engineering with North Carolina State University, Raleigh, NC, USA. He has authored or co-authored over 400 publications on topics related to microwave and millimeter-wave systems, nonlinear RF effects, circuit–electromagnetic–acoustic interactions, RF behavioral modeling, RF circuit simulation, high-speed digital design, and RF/microwave design methodology. He has co-authored *Foundations of Interconnect and Microstrip Design* (Wiley, 2000), *Multifunctional Adaptive Microwave Circuits and Systems* (SciTech, 2009), and *Microwave and RF Design: A Systems Approach* (SciTech, 2010). Dr. Steer was a Secretary of the IEEE Microwave Theory and Techniques Society (IEEE MTT-S) in 1997 and was on the IEEE MTT-S Administrative Committee (1998–2001 and 2003–2006). He was the Editor-in-Chief of the IEEE Transactions on Microwave Theory and Techniques. He was a recipient of the Alcoa Foundation Distinguished Research Award of North Carolina State University (2003), the Jack S. Kilby Lecturer (2003), and the Bronze Medallion from the U.S. Army Research for Outstanding Scientific Accomplishment (1994 and 1996). He was a recipient of the Military Medal Commander's Award for Public Service from the Commanding General of the U.S. Army Research, Development and Engineering Command (2009). He shared the 2010 Microwave Prize of the IEEE MTT-S for the best paper on microwave engineering published in any IEEE publication in 2009. He was the recipient of the 2011 Distinguished Educator Award of the IEEE MTT-S. He was inducted into the Electronic Warfare Technology Hall of Fame sponsored by the Association of Old Crows, and was named One of the Most Creative Teachers in the South by Oxford American Magazine.

● ● ●

AUSTIN J. PICKLES received the B.S. and M.S. degrees in electrical engineering from North Carolina State University (NCSU), Raleigh, NC, USA, in 2008 and 2009, respectively, where he is currently pursuing the Ph.D. degree.

He is a Graduate Research Assistant at NCSU.

IAN M. KILGORE (M'10) was born in Los Angeles, USA, in 1990. He received the B.S. degree in electrical engineering from North Carolina State University (NCSU) in 2013, where he is currently pursuing the Ph.D. degree.

He is a Graduate Research Assistant at NCSU.

Mr. Kilgore is a member of Eta Kappa Nu and Beta Eta Chapter.